Key Points:
- The Houston Lightning Mapping Array reveals collocated extreme lightning activity and precipitation rates during Tropical Storm Harvey
- Lightning is an adequate predictor of extreme deep convective behavior within a tropical cyclone when the mixed-phase depth is elevated

Correspondence to:
T. Logan,
tlogan52@tamu.edu

An Analysis of the Performance of the Houston Lightning Mapping Array During an Intense Period of Convection During Tropical Storm Harvey

Timothy Logan[1] (ID)

[1]Texas A&M University, College Station, TX, USA

Abstract Extreme lightning activity (~300,000 flashes) was observed by the Houston Lightning Mapping Array (HLMA) network during Tropical Storm Harvey on August 26, 2017–August 27, 2017. There was an overall weak correlation between the lightning flash and precipitation rates ($R = 0.14$; $p \sim 0.17$) likely due to feeder bands transitioning between deep and shallow convection. The peak precipitation rate (14.2 mm hr^{-1}) lagged the peak lightning flash rate (~18,000 flashes [30 min]$^{-1}$) by 7 h. Adjusting for the lag, the correlation increased to 0.71 ($p < 0.01$) indicating a relationship between the uptick in lightning activity in the convective feeder bands and the resulting heavy precipitation during episodes of shallow convection. Peak lightning flash extent densities of 12.4 km^{-2} min^{-1} were spatially collocated with precipitation rates exceeding 9 mm hr^{-1}. NEXRAD reflectivity data featured 30 dBZ echo heights in excess of 10 km that were collocated with peak lightning flash extent densities exceeding 3 km^{-2} min^{-1}. The NEXRAD specific phase (k_{dp}) and differential phase (Z_{dr}) dual-polarization products were highest ($\geq 2°$ km^{-1} and dB) below the melting layer (4.6 km) indicating heavy precipitation and strong updrafts. Negative k_{dp} and Z_{dr} values ($\leq -0.15°$ km^{-1} and dB) collocated with the peak lightning flash extent density altitudes indicated ice particle generation which likely augmented the charge separation process. This is likely the first time a major tropical cyclone has occurred within the confines of a lightning mapping array. The lightning data, when used synergistically with radar and precipitation data, can adequately quantify tropical convection exhibiting an elevated mixed-phase depth.

Plain Language Summary Hurricane Harvey made landfall as a Category 4 storm (60 m s^{-1} maximum sustained wind speed) on the evening of August 25, 2017 (0300 UTC August 26, 2017) near the Texas Gulf Coast city of Port Aransas. Over a 2-day period (26–27 August 2017), Tropical Storm Harvey devastated the Houston Metropolitan Area with intense convection and historic flooding. Over 700 mm of rainfall was recorded during the 48-h period. Harvey was completely within the confines of the Houston Lightning Mapping Array (HLMA) Network which recorded nearly 300,000 lightning strikes. The most intense lightning occurred during the evening hours of August 26, 2017 (0100–0600 UTC August 27, 2017). Peak lightning flash rates were in excess of 18,000 flashes per half hour which preceded extreme rain rates of 14 mm hr^{-1} that led to devastating flooding south and east of Houston. Radar data illustrated areas of intense convection that were collocated with intense, high-altitude (10–15 km) lightning activity. Later during the day on August 27, 2017, the lightning activity subsided while the rain rate increased due the intense deep convection transitioning to shallow, but intense convection.

1. Introduction

Tropical cyclones are capable of inflicting considerable damage to coastal and inland regions (Brauer et al., 2020; DeMaria et al., 2012). The damage typically comes from severe winds and storm surge while inland flooding is a large concern particularly during the tropical storm stage. On August 23, 2017, the remnants of a previous tropical cyclone (Harvey) rapidly re-intensified over the western Gulf of Mexico. During the evening of August 25, 2017 (0300 UTC August 26, 2017), Hurricane Harvey made landfall along the Texas Gulf Coast near Port Aransas as a Category 4 storm (recorded peak wind speed at nearly 60 m s^{-1}). Harvey weakened within hours of landfall and was downgraded to a tropical storm. A synoptic combination of the position of two upper level high pressure systems and anticyclonic wind patterns to the west and east of Harvey caused the tropical storm to slowly drift and meander eastward for several days along the Gulf Coast in Southeast Texas (Figure 1).
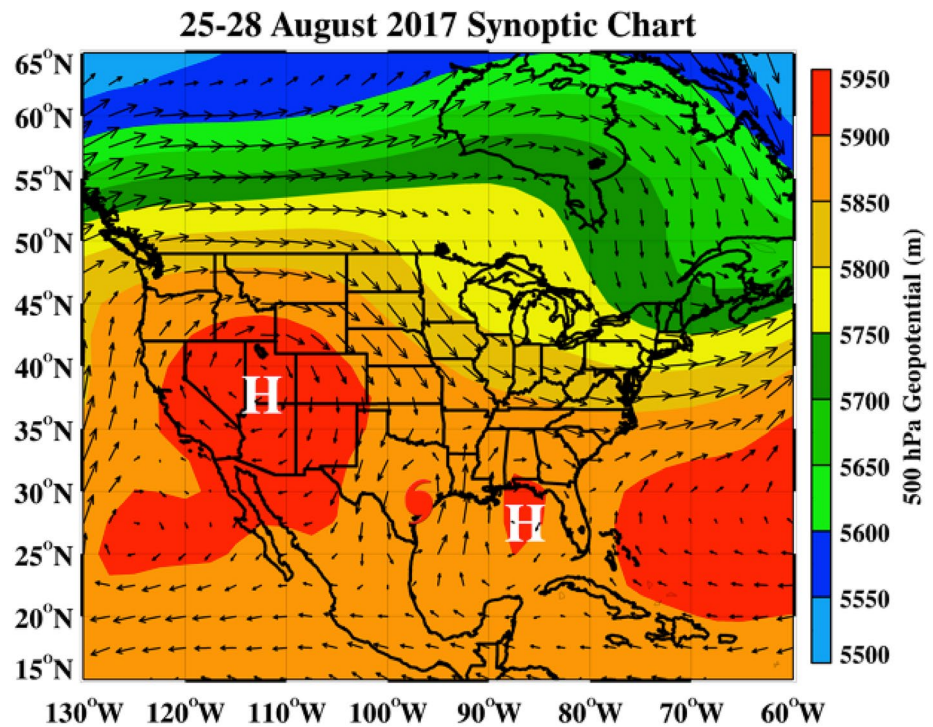
Figure 1. Tropical Storm Harvey in relation to two synoptic 500 hPa ridges (white "H"). Note the steering wind currents around the upper level high pressure systems which act to slow the propagation of Harvey to the east. Note the influence of the Bermuda High in the easternmost part of the domain.

As a result, the Buffalo and Brays Bayous, two major bodies of water that run through the city of Houston, had overflowed and impacted numerous urban areas, roads, and businesses causing closures and evacuations. The release of water from dams west of Houston also caused extensive flooding, especially in and around the Barker Reservoir. Furthermore, commerce was disrupted along a major east-west Gulf Coast transit corridor which connects Houston and points west with New Orleans and points east for several weeks due to impassable, inundated roads. The majority of the flooding was caused by a combination of intermittent deep convection within the slow-moving feeder bands that were positioned over Southeast Texas (Brauer et al., 2020). In addition, there was appreciable flooding in regions that exhibited broad areas of long-lived shallow convection which is certainly typical of tropical cyclones (Brauer et al., 2020; DeMaria et al., 2012).

Tropical cyclones can exhibit notable changes in lightning activity in and around the eyewall region which gives clues as to whether they are undergoing rapid intensification or weakening (Shao et al., 2005; Solorzano et al., 2018; Xu et al., 2017; W. Zhang et al., 2015). In addition, studies have suggested a fair to moderate, statistically significant correlation between lightning activity and rain rate within the feeder bands that dynamically and thermodynamically support eyewall convection (DeMaria et al., 2012; Shao et al., 2005; Solorzano et al., 2016, 2018; Stolz et al., 2014; Xu et al., 2017). As the convection around the eyewall intensifies, billowing updrafts can loft cloud condensation nuclei (CCN) and cloud droplets well above the melting layer which initiates the cold rain process (Shao et al., 2005; Solorzano et al., 2018; Xu et al., 2017). Supercooled liquid water droplets and ice particles (e.g., snow, graupel, and hail) are the primary products of this process and are needed for the non-inductive charge mechanism responsible for cloud electrification (Fuchs et al., 2015; Solorzano et al., 2018; Takahashi, 1978; van Lier-Walqui et al., 2016). There is limited evidence of additional charging mechanisms via the warm rain process where much of the deep convective cloud is below the melting layer (Saunders, 1993). Saunders (1993) pointed out that warm clouds could undergo convective charging except for instances where clouds are short-lived (~10-min lifetime). However, it is possible in the case of Harvey to have the warm cloud electrification if there is long-lived, shallow convection within the feeder bands.

Lightning detection networks are crucial in analyzing the behavior of electrically active, deep convective storms over land and ocean (Fridlind et al., 2019; Shao et al., 2005; Solorzano et al., 2018; Stolz et al., 2014; Thornton et al., 2017; Xu et al., 2017; Zhang et al., 2015). There are various ground- and space-based networks that are capable of analyzing lightning activity. The National Lightning Detection Network (NLDN) is an often-used ground-based network that is, capable of giving information on the location, time of flash, type of flash, peak current, and polarity of lightning flashes (Calhoun et al., 2013; Cummins & Murphy, 2009; Logan, 2018; Mecikalski & Carey, 2018; Stolz et al., 2014). In fact, there is evidence that the peak current and polarity are related to not only updraft strength but cloud microphysics as well (Fan et al., 2015; Logan, 2018; Lyons et al., 1998; Thornton et al., 2017; van Lier-Walqui et al., 2016; Y. Zhang et al., 2019). The World Wide Lightning Location Network (WWLLN) is a global network of sensors capable of detecting lightning activity within several hundred kilometers of a given sensor (Solorzano et al., 2018; W. Zhang et al., 2015). The WWLLN is useful in examining and analyzing lightning activity over remote ocean and land areas. The Geostationary Lightning Mapper (GLM), onboard the Geostationary Operational Environmental Satellite (GOES) platform, is an optical sensor that can track the evolution of electrical activity during the development of thunderstorms (E. Bruning et al., 2019). Although the sensor cannot detect all forms of lightning from space, it is extremely useful as a prognostic tool for forecasting thunderstorm behavior (Borque et al., 2020; E. Bruning et al., 2019; Xu et al., 2017). Lightning mapping arrays (LMAs) can analyze the evolution of a lightning flash by detecting and grouping individual electromagnetic pulses in the very high frequency (VHF) range (60–66 MHz) in space and time (E. C. Bruning & MacGorman, 2013; Chmielewski et al., 2016; Fridlind et al., 2019; Fuchs et al., 2016; Ren et al., 2018; Rison et al., 1999; Thomas et al., 2004; Weiss et al., 2018).

The Texas Gulf Coast is a major urban/industrial region that is, impacted by mesoscale and synoptic weather patterns (e.g., sea breeze thunderstorms, frontal passages, and tropical systems) throughout the year (Fridlind et al., 2019; Levy et al., 2013; Orville et al., 2001). Houston ranks as the fourth largest city in the United States in terms of population and is a major metropolitan hub for residential, medical, tourism, and commercial activities. In addition, the Houston Metropolitan Area is not only home to numerous petrochemical refineries and service facilities, but also several major shipping ports with direct access to the Gulf of Mexico (Fan et al., 2006; Fridlind et al., 2019; Levy et al., 2013; Orville et al., 2001). The Houston LMA (HLMA) observed the lightning activity of Harvey from landfall on August 26, 2017 until its eventual exit from Texas on August 30, 2017. Intense convective feeder bands from Harvey were already being observed by the HLMA just prior to making landfall during the late hours of August 25, 2017. It should be noted that there were numerous accounts on social media of vivid and frequent lightning during the evening of August 26, 2017 (0100–0300 UTC August 27, 2017). Lightning activity from past major tropical cyclone events was not as well documented as with Harvey and thus serves as a major motivation for this study. Moreover, this is likely the first time a major tropical cyclone has occurred within the confines of a LMA. The historic flooding that occurred several hours after the extreme lightning event serves as an additional area of focus.

Thus, this study presents a unique opportunity to use lightning behavior observed by the HLMA to investigate (a) the evolution of a tropical cyclone within a transitional marine/continental setting as well as (b) the impacts of a tropical cyclone on a major metropolitan area. This study seeks to address two scientific questions: SQ1: What was the nature of the meteorological conditions that resulted in the observed anomalous lightning behavior during Tropical Storm Harvey? and SQ2: How can lightning activity retrieved from the HLMA be used to quantify the magnitude of convection with respect to precipitation intensity and flooding during Tropical Storm Harvey?

Section 2 discusses the methodology of using the HLMA to illustrate the lightning behavior of Harvey during an intense period of convection and flooding. The synergistic use of additional datasets such as precipitation and dual-polarization radar products are also discussed. The results taken from three cases of extreme lightning and precipitation during Harvey are presented in Section 3. A discussion of the results addressing the two scientific questions is presented at the end of the section. Section 4 contains a brief summary and a focus for future research applications of the HLMA.
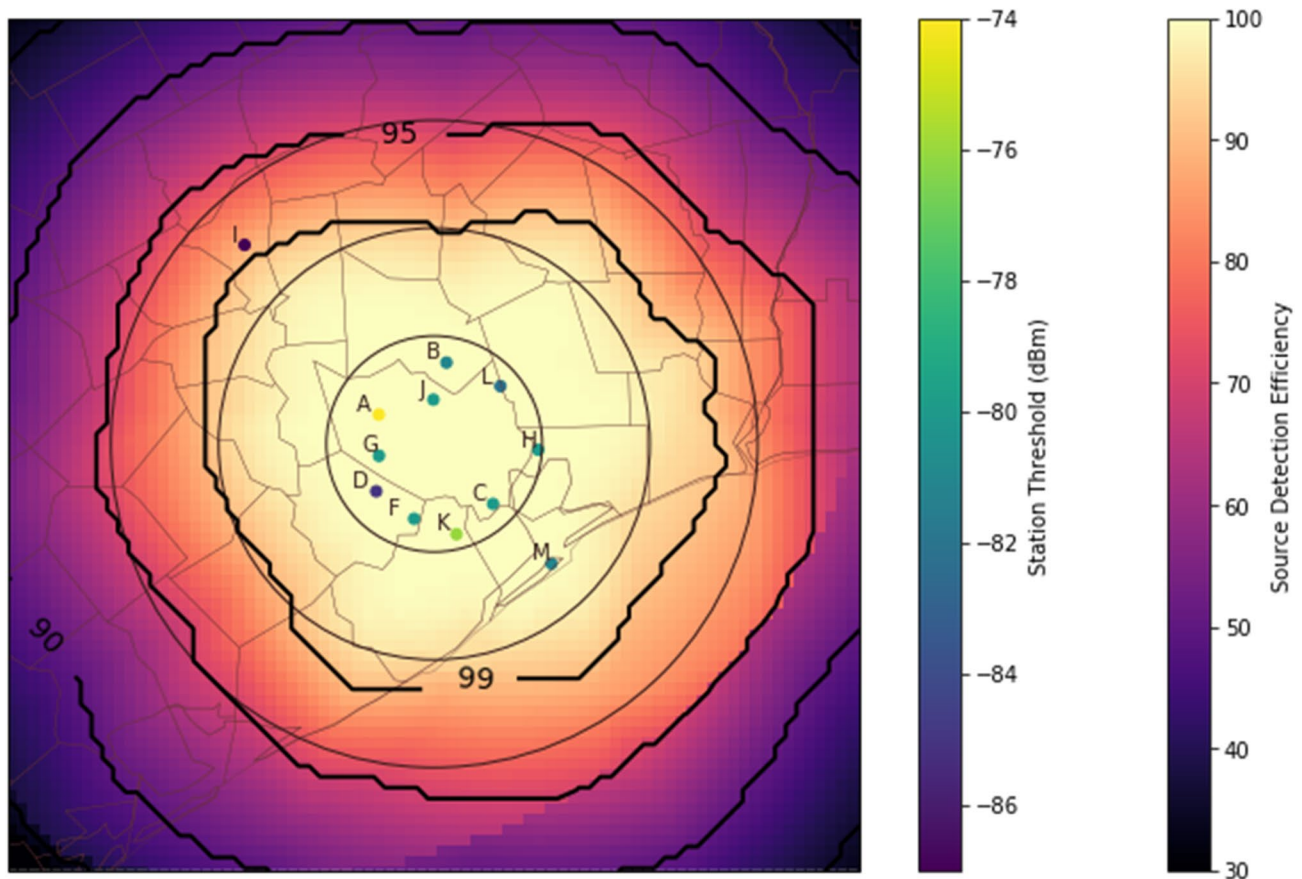
Figure 2. The Houston Lightning Mapping Array (HLMA) Network consists of 12 sensors that detect VHF sources emanating from electrified clouds. Range rings from innermost outward represent 50, 100, and 150 km radius of detection from centroid. The HLMA range of detection comprises much of the Houston Metropolitan Area and the adjacent coastal waters of the Gulf of Mexico. There is a near 100% detection efficiency within 100 km of the HLMA centroid (courtesy of Eric Bruning, Texas Tech University).

2. Data and Methodology

The spatial domain of study is defined as a rectangle bounded by 27°–32°N and 93°–98°W which encompasses the inner 100 km radius of the HLMA as well as the entire Houston Metropolitan Area extending out over the Gulf of Mexico (Figure 2). Three cases that occurred on August 27, 2017 were chosen in this study based on the flash rates observed by the HLMA. Two cases represented the highest peak flash rates while one case represented the lowest flash rate to serve as a contrast. The cases are described as follows: the period of the most intense convection and lightning activity (0130–0230 UTC; Case I), the development of an intense deep convective "mini-supercell" (0500–0600 UTC; Case II), and a broad area of intense convection exhibiting less frequent lightning but anomalous rain rates (1100–1200 UTC; Case III).

2.1. Houston Lightning Mapping Array (HLMA) Network

The HLMA network initially consisted of 10 sensors capable of detecting VHF source emissions (60–66 MHz) from thunderstorms in three spatial dimensions in real-time (Cullen, 2013; Thomas et al., 2004). A time-of-arrival method based on the measured time for the VHF source pulse to reach the sensors is used to calculate the position of the source in terms of longitude, latitude, and altitude (Cullen, 2013; Fuchs et al., 2016; Thomas et al., 2004). The sources originate from the breakdown process of lightning in which the charges flow from the point of initiation and propagate from cloud to ground (CG) or within clouds (IC) (Cummins et al., 2000; Rison et al., 1999; Thomas et al., 2004). The HLMA network first went online in

2011 to replace the defunct Lightning Detection and Ranging (LDAR) network (e.g., Cullen, 2013; Koshak et al., 2007).

Several studies have developed methodologies to decrease the amount of spatial uncertainty since measurement errors tend to increase rapidly with increasing distance between the VHF sources and the sensors (Chmielewski et al., 2016; Thomas et al., 2004; Weiss et al., 2018). Rison et al. (1999) found that the errors increase with the square of the range between the source and sensor. For the HLMA, Cullen (2013) demonstrated that due to the Earth's curvature, only the most powerful sources are detected by the sensors at ranges beyond 100 km from the HLMA centroid (located at 29.76°N, 95.37°W) which can bias the data retrievals. Thus, in 2012, two additional sensors were added: 130 km north (College Station) and 75 km south (Galveston) of the HLMA centroid. This significantly improved the detection efficiency to near 100% within 100 km of the centroid and increased the accuracy of the VHF sources by reducing the height uncertainty from 200 m to less than 20 m (Chmielewski et al., 2016; Cullen, 2013). In addition, this expanded the coverage of the HLMA, especially out over the Gulf of Mexico. In particular, the Galveston sensor ("M" in Figure 2) can aid in detecting electrically active marine deep convection. Therefore, this study adopts the data correction methods developed by Cullen (2013) and Ren et al. (2018) and primarily focuses on the strongest lightning events during Harvey which occurred within 125 km of the HLMA network center.

The VHF sources are then processed into flashes and flash extent via algorithms discussed in the McCaul et al. (2009), Bruning (2013), Fuchs et al. (2015), Ren et al. (2018), and Fuchs and Rutledge (2018) studies. The flash product has a spatial resolution of (0.01 × 0.01). Note that the flash level data will be directly compared to the precipitation rain rate product which has a temporal resolution of 30-min. The flash rate is used in this study to determine the active periods of the tropical cyclone within the full range of detection of the HLMA. It is assumed that greater than 99% of all flashes are detected within 125 km of the HLMA centroid (e.g., Fuchs et al., 2015; Ren et al., 2018). Figure 2 shows that nearly 90% of the flashes can be detected within 300 km of the centroid and thus, the flash and flash extent products for much of the tropical cyclone can be analyzed without greatly sacrificing data quality.

The lightning flash extent density (processed via an open source program "lmatools"; Bruning, 2013; Fuchs et al., 2015) is more descriptive of the convective nature of storms than solely relying on the VHF source data (Mecikalski & Carey, 2018; van Lier-Walqui et al., 2016). That is, higher flash rates in conjunction with smaller flash extents (~3 km) typically denote deep convection and turbulence while longer flash extents (>3 km) and lower flash rates can denote more stratiform or shallower convection (DiGangi et al., 2016; Fuchs & Rutledge, 2018). The flash products rendered by the "lmatools" algorithm have a spatial resolution of 0.0103 × 0.0103 (1 km^2) and temporal resolution of 1-min. The flash density methodology used in this study follows several previous studies such as Fuchs et al. (2015, 2016), and DiGangi et al. (2016) where a spatial threshold of 3 km and temporal threshold of 0.15 s is used to constrain the lightning flash. Note that there has yet to be a study to determine a suitable threshold for the Houston Lightning Mapping Array and will be a thus be a focus of future work.

2.2. NEXRAD

The network of NOAA Weather Surveillance Radar 1988 Doppler edition (NEXRAD) (Crum & Alberty, 1993) has greatly added to the meteorological body of knowledge since its upgrade during the past decade. The network consists of 160 radar sites with a maximum range of coverage of 460 km. The radar scans a volume of atmosphere from a level of 0.5° to the horizontal up to 5°, typically having a 10-min resolution during clear air mode or 5-min resolution in storm mode. The scan can give an adequate illustration of various atmospheric features (e.g., precipitation events, smoke/ash particles from fires, flying animal migrations, etc.). The NEXRAD platforms have since been upgraded to dual-polarization (dual-pol) capabilities which greatly enhanced their ability to identify liquid and frozen hydrometeor characteristics such as intensity, type, concentration, and orientation.

The major NEXRAD products used in this study include: reflectivity data, and the dual-pol products of specific differential phase (k_{dp}), differential reflectivity (Z_{dr}), and cross-correlation (ρ_{hv}). The k_{dp}, Z_{dr}, and ρ_{hv} products illustrate the vertical and horizontal interaction of the radar beam with hydrometeors (Brauer

et al., 2020; Cifelli et al., 2010; Cui et al., 2019; Fridlind et al., 2019; Kumjian, 2013; Li & Mecikalski, 2012; Tian et al., 2020). For example, a falling raindrop is considered to have a larger horizontal than vertical semi-axis ("hamburger shape") with positive k_{dp} and Z_{dr} values. Graupel and hail are typically symmetric about all axes (spherical shape) and generally have k_{dp}/Z_{dr} values near zero and ρ_{hv} values approaching unity. Smaller ice particles such as snowflake needles and columns will have larger vertical than horizontal dimensions and typically have negative k_{dp}/Z_{dr} values with ρ_{hv} values less than unity. Strong precipitation activity and updraft intensity can also be inferred by k_{dp} (Z_{dr}) values exceeding $2°$ km^{-1} (dB) while ρ_{hv} values are typically less than unity due to a mixture of hydrometeor types and orientations.

The evolution of deep convective cloud microphysics can be demonstrated by dual-pol radar products during the first stages of lightning development (Fridlind et al., 2019; Wiens et al., 2005). As hydrometeors are carried upward through the atmosphere by strong updrafts (>10 m s^{-1}), they can grow by condensation, collision, and coalescence. The major tenet of the non-inductive charge mechanism is that hydrometeors are lofted above the $-10°$C isotherm and become ice particles. The larger ice particles carry a positive charge and fall through the cloud and collide with small, negatively charged ice particles in the presence of supercooled liquid water thereby exchanging charges. The now positively charged particles are carried up to the top of the cloud by strong convective updrafts (>10 m s^{-1}) while during the process of gravitational settling, the negatively charged particles will occupy the lower part or base of the cloud (assuming they have not yet exited).

Hints of this process can be elucidated by using the NEXRAD dual-pol products to illustrate (a) regions of large concentrations, (b) sphericity, and (c) spatial orientation of the hydrometeors (Kumjian, 2013; van Lier-Walqui et al., 2016). GridRad, a gridded NEXRAD product, can render the reflectivity, Z_{dr}, k_{dp}, and ρ_{hv} products into plan and cross-section views (Cooney et al., 2018; Homeyer et al., 2017; D. L. Solomon et al., 2016; Starzec et al., 2017). The GridRad data have a temporal resolution of 5-min and spatial resolution of ($0.02 \times 0.02 \times 1$ km). GridRad is used to quantify the evolution of the deep convective precipitation magnitude and altitude in synergy with the flash extent density products.

2.3. GPM Precipitation Data

The Global Precipitation Measurement mission (GPM) is a joint venture between the National Aeronautics and Space Administration (NASA) and the Japan Aerospace Exploration Agency. It has been collecting critical precipitation data with respect to extreme precipitation events since 2014 (Skofronic-Jackson et al., 2018). The Integrated Multi-satellite Retrievals for GPM (IMERG) product is used in this study to quantify areas of intense rainfall and rain rate with respect to lightning flash behavior. The IMERG product has a spatial resolution of 0.1×0.1 with a 30-min temporal resolution (Skofronic-Jackson et al., 2018). Uncertainties due to bias and random errors are not expected to be higher than 25% at rain rates of 10 mm hr^{-1}. As previously mentioned, the HLMA flash rate data, when compared with GPM retrievals, are grouped into 30-min bins rather than the typical 1-min resolution.

3. Results

3.1. Meteorological Conditions

Balloon-borne instrument measurements provided by the National Oceanic and Atmospheric Administration (NOAA) were used to provide information regarding the dynamic/thermodynamic environment within the domain of study. The sounding data (not shown) were obtained from the Plymouth State University weather center (https://vortex.plymouth.edu). The 1200 UTC August 26, 2017 Lake Charles (LCH) sounding, located roughly 210 km east of Houston, showed a surface-based convective available potential energy (SBCAPE) value of nearly 1,800 J kg^{-1} which indicated an adequate thermodynamic environment for deep convective development (e.g., vigorous lifting of moist air parcels). The moisture and temperature variables also provided evidence for an unstable environment with precipitable water vapor (PWV) values exceeding 60 mm and surface temperatures in excess of 25°C.
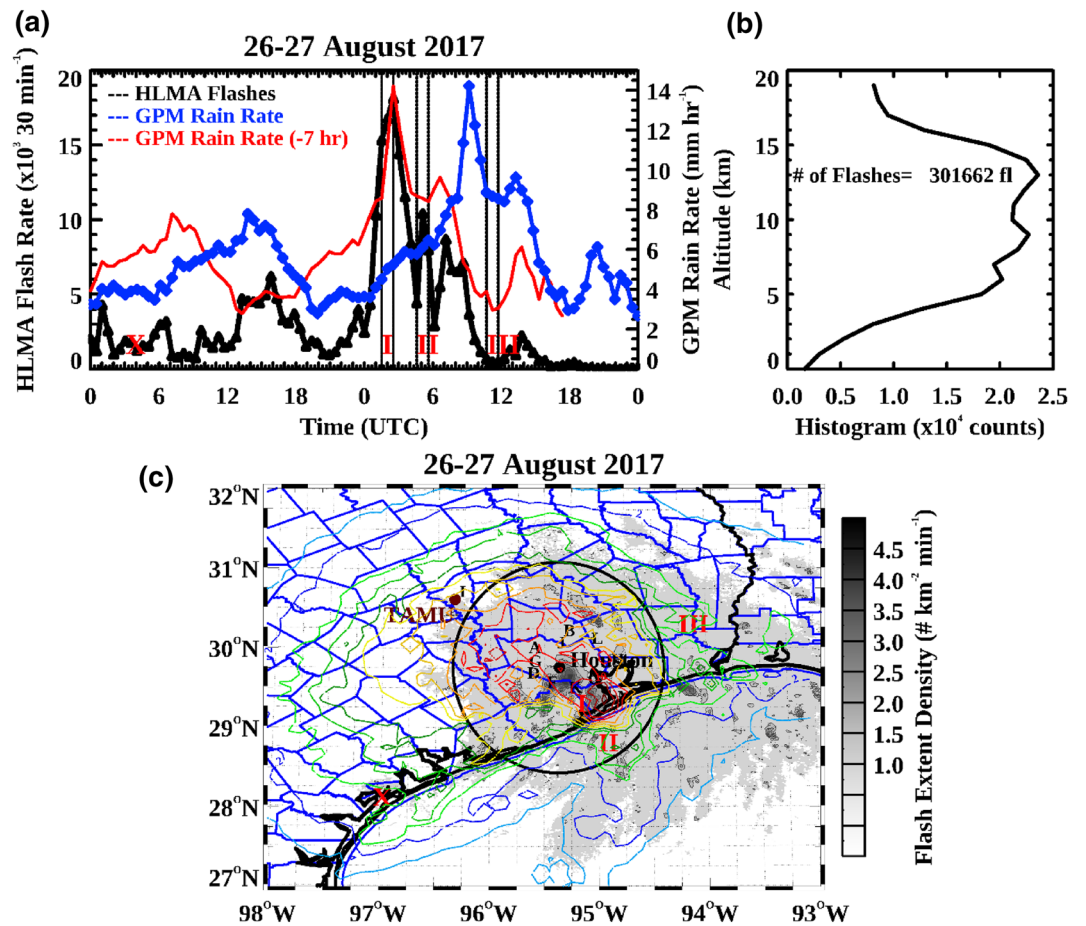
Figure 3. (a) Time series of HLMA flashes (# 30 min^{-1}) (black line), GPM rain rate (mm hr^{-1}) (blue line), and GPM rain rate shifted 7 h to account for lag (red line). The case studies discussed in this study are noted with I, II, and III. Hurricane Harvey made landfall at approximately 0300 UTC on August 27, 2017 (red "X"). (b) Altitude-histogram of lightning flash counts and total amount of flashes. (c) Plan view of 48-h lightning flash extent density with GPM rain rate contours (1 mm hr^{-1} intervals) overlain. The most extreme lightning activity occurred within the 100 km radius of detection of the HLMA network (black circle). Note the location of the lightning hotspots which serve as the basis for the case studies. The sensor locations (capital letters) are noted.

The surface wind direction was predominately out of the southeast with a speed maximum roughly 600 m AGL which aided in advecting boundary layer air parcels rich in Gulf moisture into the region. The bulk shear was roughly 12.5 m s^{-1} while the low- (0–1 km) and mid-level (0–6 km) wind shear quantities were modest (<10 m s^{-1}) indicating a possible multicellular storm mode. Furthermore, given the clockwise wind profile, developing storms could likely have rotation which was evident from the two reports of EF1 rated tornadoes (wind speeds approaching 50 m s^{-1}) at 0500 UTC on August 27, 2017. The LCH sounding further indicated that the position of the melting layer height was at around 4.6 km while the height of the −30°C (−40°C) isotherm was located at roughly 10 km (11 km) suggesting a deep mixed-phase layer (Stolz et al., 2014). Note that a stationary front propagated southward and interacted with the tropical storm and likely provided additional lifting of the moist air parcels.

3.2. Lightning Flash Density, Flash Rate, and Precipitation

Nearly 300,000 flashes were identified by the HLMA in addition to a rain amount of ~700 mm during the 48-h study period. Approximately 62% of those lightning flashes (~188,000) occurred on August 27, 2017. Figure 3a shows the time series of the HLMA lightning flash rate and GPM precipitation. The lightning

flash rate is reported in the same temporal scale as the GPM data in order to perform a representative statistical analysis of the relationship between the two measurements. The first area of peak lightning flash density (Case I) occurred between 0130 and 0230 UTC on August 27, 2017 where flash rates exceeded 18,000 flashes $(30 \text{ min})^{-1}$. The peak rain rate was 5.6 mm hr^{-1} during this period. After 0300 UTC, there was a sharp decline in lightning flash rate combined with a moderate increase in rain rate. The flash rate increased a second time between 0500 and 0600 UTC when a second area of peak lightning flash density (Case II) was observed. The peak flash rate was nearly 11,000 flashes $(30 \text{ min})^{-1}$ along with a peak rain rate of 6.5 mm hr^{-1}. Lightning flash rates continued to decline after 0600 UTC, though three additional peak flash rates exceeding 5,000 flashes $(30 \text{ min})^{-1}$ were observed. The peak rain rate of 14.2 mm hr^{-1} occurred around the same time as the last relative flash rate peak ($\sim$6900 $[30 \text{ min}]^{-1}$) at 0900 UTC. Between 1100 and 1200 UTC (Case III), the lightning flash rates fell below 50 $(30 \text{ min})^{-1}$ while the rain rate declined below 10 mm hr^{-1}.

A cross-correlation analysis of the lightning flash rate and rain rate (Figure 3a) revealed a weak overall correlation (*R*-value) of 0.14 (*p*-value $\sim$ 0.17). When the precipitation data were adjusted for the 7 h lag, the correlation and statistical significance increased further to 0.71 (*p*-value < 0.01). The temporal lag was likely due to: (a) the time differential between the uptick in lightning activity and the subsequent "pulsing down" of the convection and (b) the lateral movement of the strongly precipitating convective feeder band. Particularly for (a), Tian et al. (2020) found that deep convection featuring high ice water content (IWC) along with large concentrations of large ice particles (e.g., graupel and snow) exhibited enhanced precipitation rates (>4 mm hr^{-1}) after 2 h due to the time it took for the ice particles to undergo depositional growth, then fall through the deep convective cloud. Note that since lightning activity is strongly dependent on ice concentration, it is feasible that the ice particles responsible for the charge separation eventually melted as they fell below the melting layer and were converted to raindrops during (b).

Figure 3b illustrates the frequency and height distribution of lightning flash activity. There were three separate flash density peaks at 13, 9, and 6 km during the 48-h study period. Typically, lightning activity is observed between 9 and 10 km for the majority of electrified deep convective cases in and around the Houston area (Cullen, 2013). However, it is interesting to see flash density peaks exceeding 10 km during a tropical cyclone. Figure 3c shows the plan view of the lightning flash extent density product with GPM precipitation rate contours overlain. The flash extent density peak value of the study domain for the 48-h period was 5.1 $km^{-2} \, min^{-1}$. Cases I and II were evident in two flash extent density maxima and were nearly spatially collocated with the most intense precipitation rates. Case I was located within a broad 9 mm hr^{-1} precipitation contour while Case II denoted the maximum southeast of Houston that was located just west of the 12 mm hr^{-1} precipitation maximum (most extreme rain rate). Moreover, closer inspection revealed that the highest contour levels were "downwind" of the lightning flash extent density maxima which suggested a temporal lag between extreme lightning activity and extreme precipitation. Hence, NEXRAD dual-pol products are used in the following section to further quantify the spatial and temporal relationship of flash extent density height with respect to the behavior of the hydrometeors (liquid and frozen) within the convection.

3.3. NEXRAD Reflectivity Cross-Section Time Series

Figure 4 shows the time series of the maximum cross-section NEXRAD reflectivity echoes binned into four heights: melting layer (4.5–6 km), mid-troposphere (6–8 km), upper-troposphere (8–10+ km), and anvil/glaciation layer region (≥10 km). This study adopts the threshold used in Logan (2018) where the 30 dBZ echo height denotes the potential of lightning activity. As a "control" the melting layer height bin is assumed to have the highest overall reflectivities since much of the observed precipitation should be most intense below this level. In fact, the melting layer bin seldom declined below a maximum reflectivity of 40 dBZ during the entire study period. The maximum melting bin reflectivity exceeded 50 dBZ between 0100 and 0200 UTC August 27, 2017 just after 0130 UTC. The mid- and upper-troposphere bins remained below 40 dBZ throughout August 26, 2017 and exceeded 40 dBZ between 0200 and 0400 UTC indicating intense convective activity in the upper levels of the atmosphere. Echo heights above 10 km exceeded 35 dBZ twice from 0200-0600 UTC which overlapped with the period of the other three bins further indicating extreme deep convective activity within the feeder bands. There were several other peaks in the bins above the
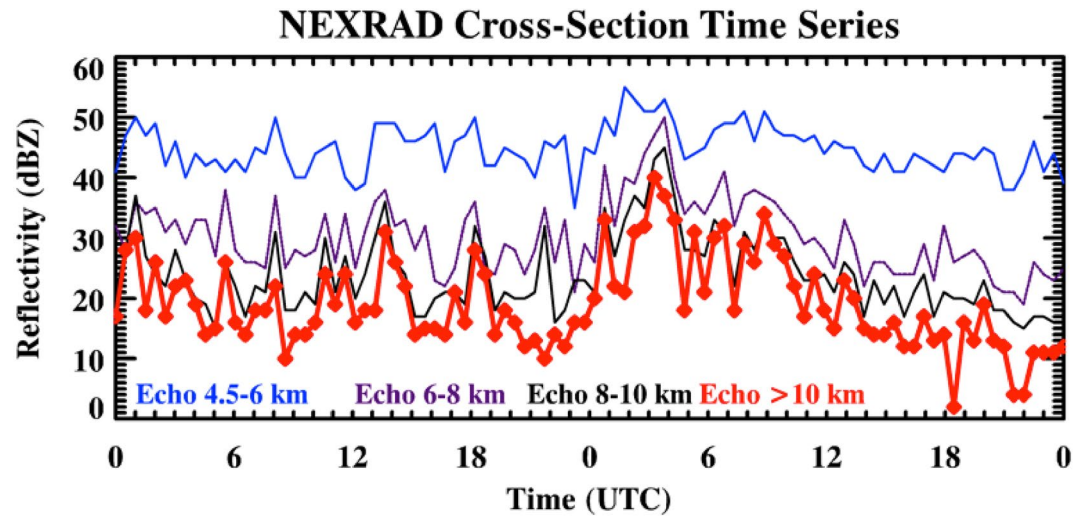
Figure 4. Maximum cross-section NEXRAD reflectivity echo heights binned into four levels: melting layer height (Echo 4.5–6 km), mid-troposphere (Echo 6–8 km), upper-troposphere (Echo 8–10 km), and anvil/glaciation level (Echo > 10 km). Note the anvil/glaciation level bin exceeded 35 dBZ between 0100 and 0400 UTC denoting vigorous deep convection from Harvey. After 0900 UTC, all reflectivity heights above the melting layer declined while the melting layer reflectivities remained moderately convective.

melting layer exceeding 30 dBZ, most notably at 0800 UTC which was an hour prior to the time of observed peak rain rate and lightning flash rate peak (see Figure 3a). After 1100 UTC, there was an overall decrease in all reflectivity height bins except for the melting layer bin which further indicates a transition to shallow convection (Carr et al., 2017).

3.4. HLMA and NEXRAD Comparative Analysis of the Tropical Storm Harvey Cases

Figure 5 shows the plan and cross-section HLMA flash extent density and NEXRAD reflectivity for the three cases. Case I evolved from a slow-moving, convective feeder band that developed after 1900 UTC on August 26, 2017 which drifted northward while Harvey slowly drifted eastward. Several hours later (0100 UTC August 27, 2017), a broad area of deep convection developed south of Houston and exhibited reflectivities approaching 55 dBZ with a peak flash extent density of 12.4 km^{-2} min^{-1} (Figure 5a). Figure 5b shows NEXRAD reflectivities exceeding 30 dBZ above 10 km with a peak cross-section flash extent density (2.6 km^{-2} min^{-1}) located just above 15 km. In Figure 5c, the flash extent density reached a peak between 0140 and 0150 UTC just before the peak flash rate observed at 0230 UTC (Figure 3a). Case II evolved a few hours later (0500 UTC) from a "mini-supercell" located northwest of Texas City (Figure 5d). Most notably, the peak reflectivity (~50 dBZ) and plan flash extent density (9.9 km^{-2} min^{-1}) from this small area of convection was comparable to what was observed during Case I. The peak cross-section flash extent density (3.2 km^{-2} min^{-1}) was located at nearly the same height as Case I (15 km) and was collocated with reflectivities in excess of 30 dBZ (Figure 5e). Note that the rain rate contours surrounding the lightning hotspot in this case were higher than for Case I (see Figure 3c). Moreover, in Figure 5f, the highest flash extent density occurred between 0505 and 0510 UTC which is why this time will be chosen for further dual-pol analysis.

As the lightning activity declined, there was an increase in rain rate just after 0900 UTC. Furthermore, a broad area of intense convection developed and was most notable at 1100 UTC during Case III. The reflectivities exceeded 40 dBZ in much of the domain (Figure 5g) but the convection cross-section shows that the high reflectivities were confined primarily below 7 km which contrasts with Cases I and II (Figure 5h). Figure 5i shows that the most intense lightning activity for this case developed after 1150 UTC but at an altitude range of 9–12 km. As pointed out by R. Solomon and Baker (1998), shallow convection tends to reduce the chances of cloud electrification due to fewer ice particles and hence a lesser chance of collisions and exchange of charges. This was evident in that flash extent density peak values were nearly an order of
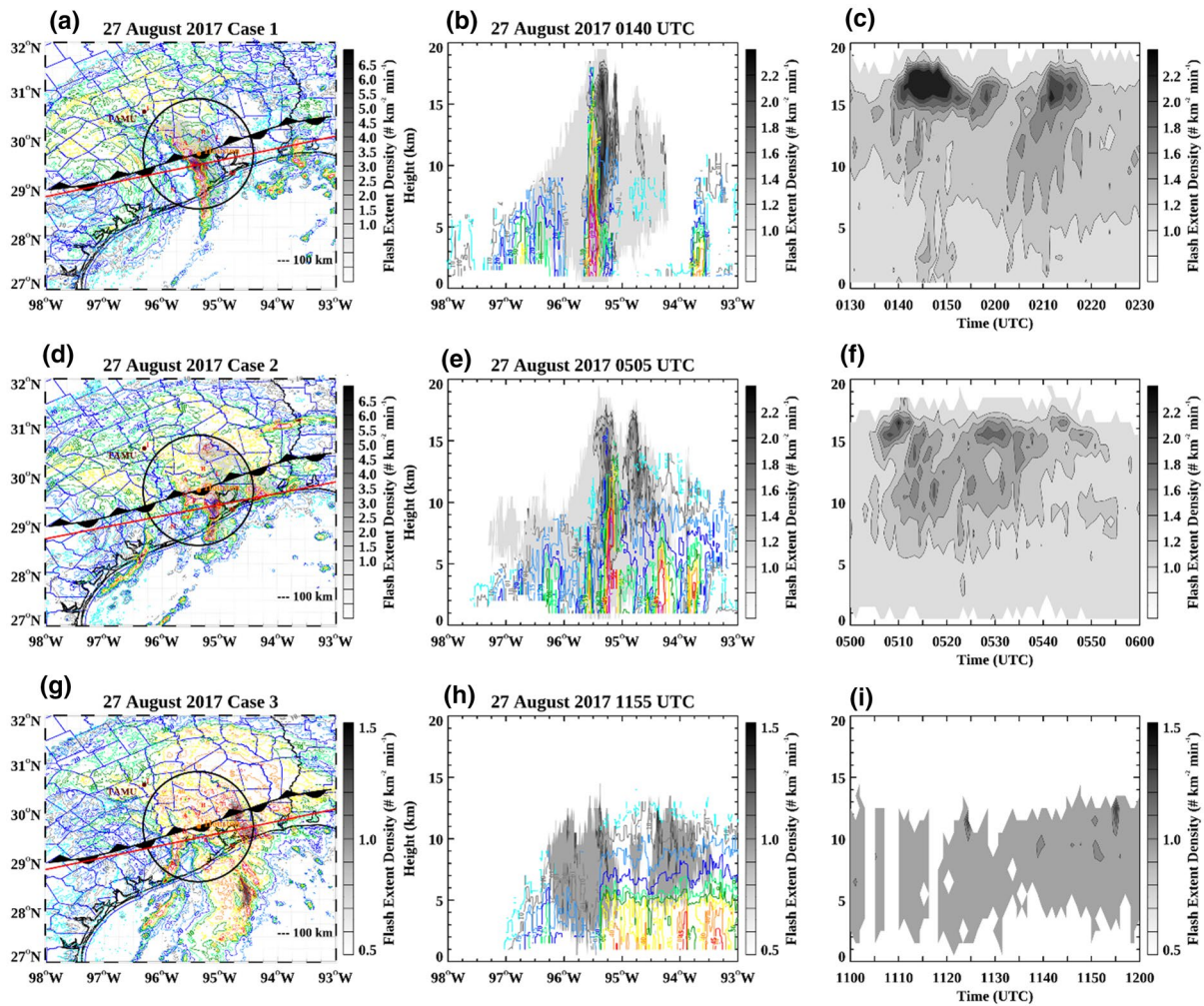
Figure 5. (a)–(c) Case I lightning flash extent density with NEXRAD contours (5 dBZ intervals) overlain. Black circle denotes 100 km radius of detection of the Houston Lightning Mapping Array network. Red line denotes cross section of NEXRAD data used for (b). The position of the stationary front is also depicted. Cross section of lightning flash extent density in the spatial (b) and temporal (c) dimensions. Same for Case II (d)–(f) and Case III (g)–(i). (b), (e), and (h) represent the volume scans during periods of most intense lightning activity.

magnitude and 50% less for the plan (4 km^{-2} min^{-1}) and cross-section (1.5 km^{-2} min^{-1}), respectively, in comparison to Cases I and II (Figures 5g and 5h).

3.4.1. Dual Polarization Products

Three NEXRAD volume scans (15 min) of k_{dp}, Z_{dr}, and ρ_{hv} dual-pol products are used to elucidate the hydrometeor and dynamical properties during the convective events (Figures 6–8). The volume scans denote the periods of peak lightning flash rates and flash extent density for each case.

3.4.1.1. Cases I and II

For Case I, deep convection was most notable at a longitude of 95.5°W along the feeder band extending from the Houston Metropolitan Area southward to the Gulf of Mexico. In Figures 6a–6c, all volume scans of the near-surface k_{dp} product showed values in excess of 2° km^{-1} up to 5 km suggesting large concentrations of hydrometeors. The values decreased to 0.25° km^{-1} at 10 km indicating smaller concentrations and sizes of ice particles. At 0140 UTC, Negative k_{dp} values ($<-0.15°$ km^{-1}) were observed just to the east at an altitude between 5 and 8 km (Figure 6a) indicating vertically oriented ice particles. A narrow area of near-surface Z_{dr} values ranging between 1 and 1.5 dB was observed below 5 km (Figures 6d–6f) from 0,140 to 0,150 UTC. At
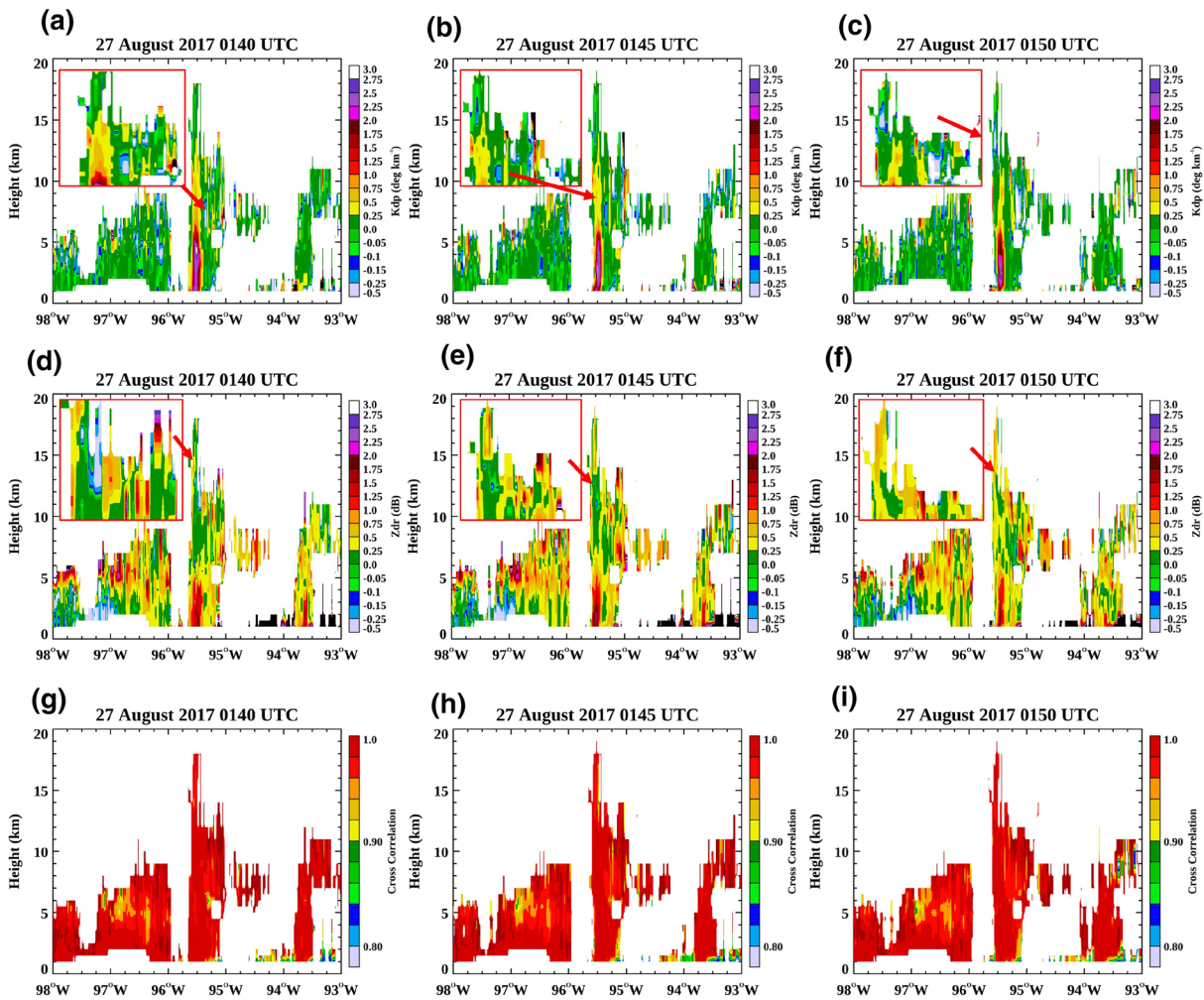
Figure 6. NEXRAD dual-polarization products of differential reflectivity (Z_{dr}), differential phase (k_{dp}), and correlation coefficient (ρ_{hv}) for the three time periods surrounding the peak in lightning activity for Case I observed in Figure 3.

0140 UTC, there was a small area of negative Z_{dr} values (<-0.15 dB) directly above the area of convection at an altitude range of 11–13 km again indicating vertically oriented ice particles (Figure 6d). However, at 0145 UTC (Figure 6e) the area of negative Z_{dr} values decreased to a negligible size which then disappeared by 0150 UTC (Figure 6f). The ρ_{hv} values were close to unity for all three volume scans (Figures 6g–6i). However, there was a small region with values below 0.9 in nearly the exact location of the negative k_{dp} values at 0140 UTC (Figure 6g) indicating hydrometeors of varying shape, size, and composition.

The elevated k_{dp} values near the surface suggest large concentrations of hydrometeors and heavy precipitation. However, negative values above the melting level (4.6 km) suggest the presence of a mixture of liquid and frozen hydrometeors. The positive Z_{dr} values denote vigorous updrafts within the line of convection while negative Z_{dr} values above 10 km denote both the presence of ice crystals and possible charging processes due to updraft turbulence. That is, the strong updrafts facilitated collisions of ice crystals in the presence of supercooled liquid water droplets and initiated the non-induction charge process. The development of regions of charge oriented the ice particles vertically and as the charge region relaxed from 0140 to 0150 UTC, the particles eventually aggregated and fell toward the lower level of the cloud via gravitational settling. The ρ_{hv} product suggested a mixture of ice and supercooled liquid water at 0140 UTC just above the melting layer which then disappeared after 0145 UTC.

Case II investigates the deep convection from a mini-supercell that formed within a convective feeder band just south of Houston. Figure 7a shows that at 0505 UTC, Case II had the highest peak k_{dp} values ($>2.75°$ km^{-1})
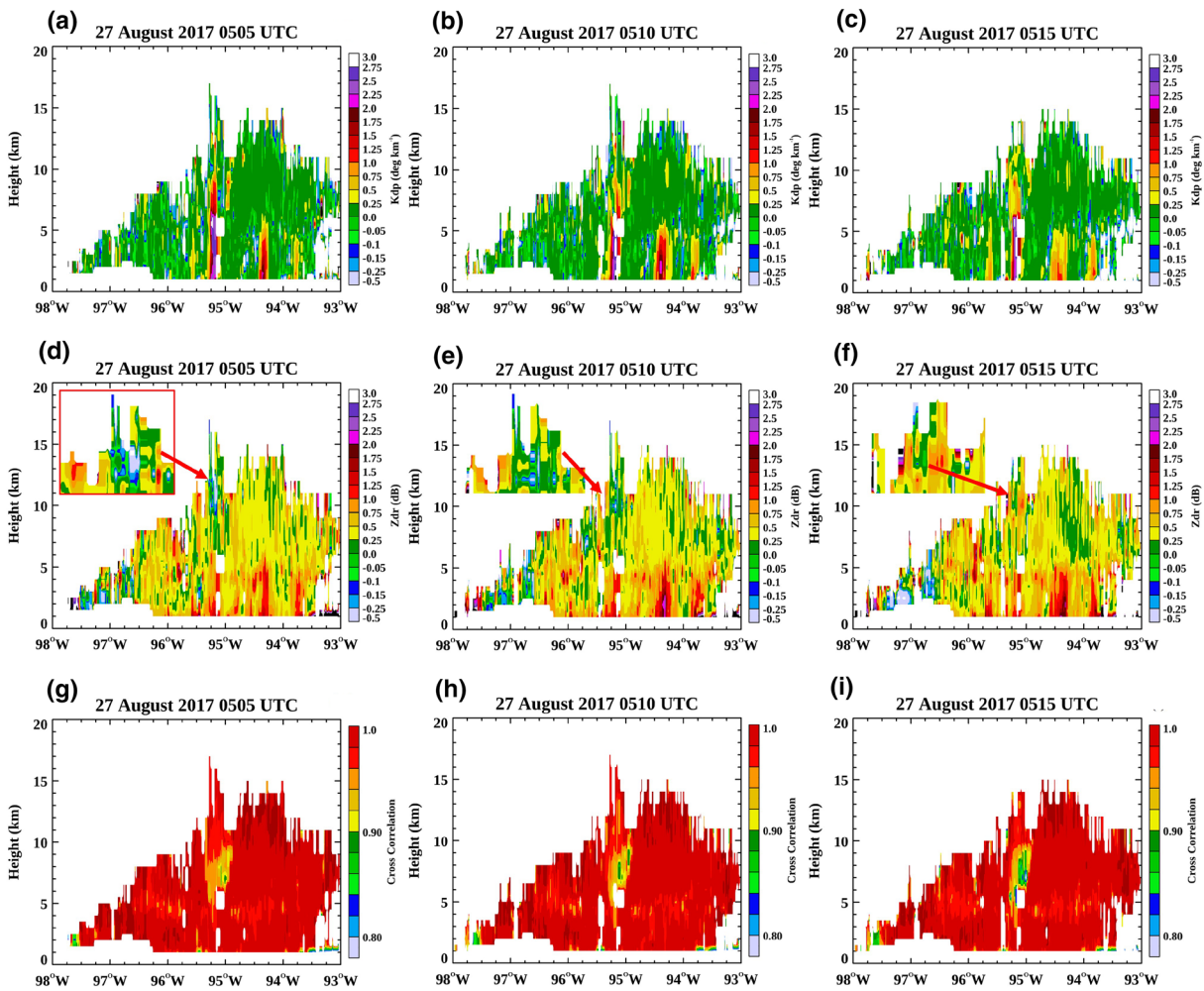
Figure 7. Same as Figure 6 but for Case II.

near the surface with values above 1° km^{-1} observed up to 9 km (~4.5 km above the melting layer). There was a small region of negative k_{dp} values ($<-0.15°$ km^{-1}) at an altitude of 8 km that disappeared in the next two scans (Figures 7b and 7c). In Figure 7d, there was a broad area of Z_{dr} values which exceeded 1.25 dB below the melting layer indicating vigorous updrafts near the surface. However, similar to Case I, there was a region of negative Z_{dr} values (<-0.15 dB) directly above the updraft (10–15 km) which suggested vertically oriented particles that were likely precipitating ice crystals (e.g., plates and/or columns). The area of negative values disappeared in the subsequent scans as the ice crystals settled out (Figures 7e and 7f). Note that this combination of negative values overlaying positive values of Z_{dr} can serve as additional evidence for an enhanced charging within the cloud that can influence the orientation of the smaller ice particles near the anvil/glaciation layer (Kumjian, 2013; van Lier-Walqui et al., 2016). A more thorough investigation of the charge layers will be performed in future HLMA studies. The ρ_{hv} values in Figures 7g–7i identified the melting level which closely matched the mean height given by the environmental sounding data (4.6 km). In addition, the region of values below 0.9 was larger than in Case II and expanded in the subsequent volume scans after 0515 UTC reaching values of 0.8 at 0525 UTC (not shown). This suggests not only a mixture of irregularly shaped frozen hydrometeors but also supports the idea of precipitation given the collocated negative Z_{dr} and elevated k_{dp} values (Kumjian, 2013). In fact, it was likely snowing at that altitude as more ice particles aggregated and descended toward the melting layer. Note that Case II occurred within a heavily industrialized area (e.g., large number of petrochemical refineries and chemical plants). Furthermore, there may have been a possible aerosol influence on the deep convective cloud microphysics (e.g., enhanced
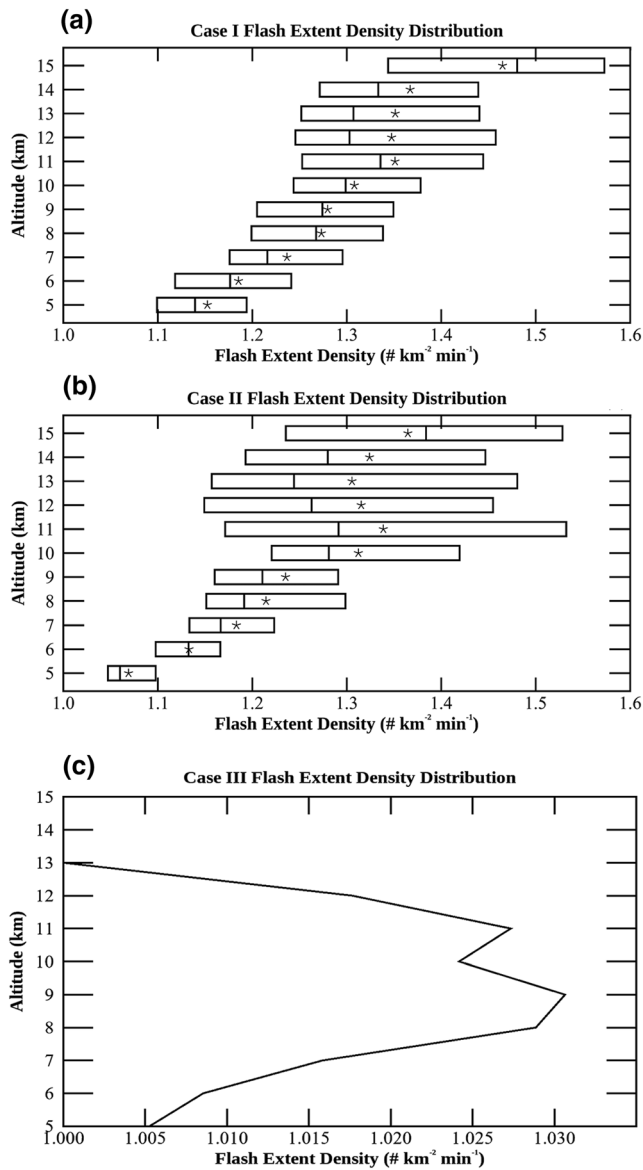
Figure 8. Cases (a) I and (b) II lightning flash extent density $(500\ \text{m})^{-1}$ boxplots along with the mean values (denoted by stars) and medians (denoted by vertical lines). Both cases show the largest flash extent values above 10 km with a maximum near 15 km suggesting intense upper troposphere electrical activity due to vigorous updrafts extending to the mid-levels of the atmosphere providing the turbulence needed to facilitate the non-induction charge mechanism between ice particles and supercooled liquid water. (c) Case III featured less intense lightning at lower altitudes than the other two cases. Note that due to many flash extent density values of near unity, no boxplot could be made.

production of ice nuclei). Hence, this case will be investigated in future studies.

The flash extent density height distribution is an additional dimension used to elucidate the high altitude lightning activity observed during Harvey (Figure 8). In Figures 8a and 8b, Cases I and II, respectively, showed a similar profile of lightning flash extent density which increased from the melting level to the −40°C level. The interquartile range (IQR) along with the mean flash extent densities steadily increased up to 11 km, then plateaued or slightly decreased before increasing to a maximum at 15 km. The mean exceeded the median in nearly all altitudes. The positive skewing and wide variability of the flash extent density data further support the idea of turbulent motions in the upper atmosphere due to vigorous updrafts leading to not only an enhancement of ice production but an enhancement of the non-inductive charge mechanism throughout the mid- and upper troposphere. Case I exhibited higher mean flash extent densities but smaller IQR than Case II. As pointed out by Mecikalski and Carey (2018), this may be a result of the different storm modes between the cases. For example, the convective feeder band from Case I resembles a linear mesoscale convective system (MCS) where the lightning is distributed along the main line of convection which stretched from Houston to several dozens of kilometers out over the Gulf of Mexico. Recall in Figure 7c, the lightning activity was the most intense at altitudes above 10 km for nearly an hour as the convective feeder band propagated eastward. Case II was a mini-supercell that formed within the convective feeder band of Case I which featured lightning activity concentrated within a smaller area. The IQR was larger for Case II primarily because of the frequent pulsing of the mini-supercell (see Figure 7f). Note that IQR was not available at all heights, namely the surface to 4 km and above 15 km owing to a lack of spread between flash extent density values (e.g., there was an abundance of zero and unity values).

3.4.1.2. Case III

Figures 9a–9c shows k_{dp} values exceeding 0.75° km^{-1} below the melting layer, in several locations east of 95°W indicating pockets of intense near-surface rainfall. Moreover, there was a broad area of k_{dp} values exceeding 0.25° km^{-1} at altitudes ranging from 5–10 km. Moderately strong, near-surface updrafts were evident given the collocated Z_{dr} values of 1.25 dB (Figures 9d–9f). In the 1155 UTC scan (Figure 9e), there was a small area of negative Z_{dr} values ($\sim$−0.15 dB) that appeared and disappeared in the next scan indicating possible charging at about 7 km which was lower than what was observed in Cases I and II. The ρ_{hv} product in Case III showed the clearest evidence of a "bright banding" feature at the melting level in all three volume scans (values of around 0.9) (Figures 9g–9i). The ρ_{hv} values of $\sim$0.95 at around 94.5°W at an altitude range of 10–15 km suggested pockets of mixed-phase hydrometeors but did not show significant particle sedimentation compared with Case II. This likely explains the less intense, lower altitude lightning observed in Figures 5h and 5i though there were widespread areas of NEXRAD reflectivities exceeding 40 dBZ (see Figure 5g). Moreover, since the highest Z_{dr} and k_{dp} values were confined below the melting layer, it was further evident that the convection during Case III was predominately shallow (Carr et al., 2017).
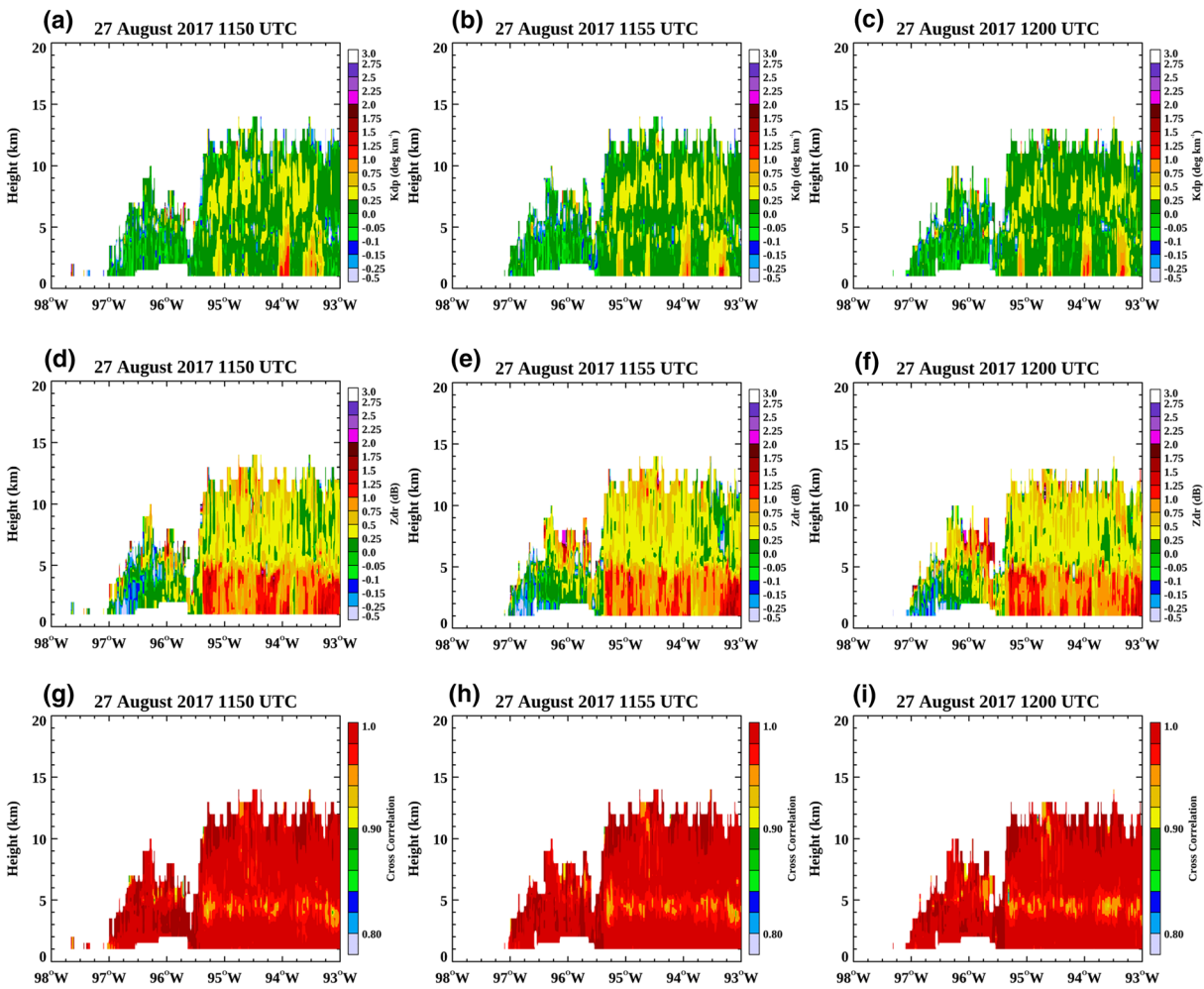
Figure 9. Same as Figure 6 but for Case III.

The mean flash extent density height distribution at 9 km for Case III was noticeably lower than Cases I and II (Figure 8c). The IQR could not be calculated since the lightning activity was much less frequent and intense during this time. However, it is interesting to point out that though the k_{dp}, Z_{dr}, and ρ_{hv} products revealed intense near surface precipitation, updrafts, and the freezing level respectively, it did not appear that significant charging was taking place within the convection during this case. In fact, it is possible that the warm cloud charging mechanism (Saunders, 1993) may have been active during this case. The intense shallow convection certainly lasted more than 10 min and was widespread within the right front quadrant of the tropical cyclone (see Figure 5g). Hence, using lightning activity as a predictor of convective strength is feasible when the convection extends well into the troposphere. Further investigation of the HLMA data may give insight to charging during periods of shallow convection. The dual-pol products and statistical values are summarized in Tables 1 and 2.

4. Summary and Future Work

After rapidly re-intensifying from tropical cyclone remnants in the Gulf of Mexico, Harvey impacted the Texas Gulf Coast region as a major Category 4 hurricane on August 26, 2017 at 0300 UTC. Harvey rapidly weakened to a tropical storm and slowly drifted eastward for several days due to two stagnant high pressure ridges located to the east and west along with weak mid-level (500 hPa) steering winds. The Houston Lightning Mapping Array (HLMA) recorded nearly 300,000 lightning flashes from intense, convective rain bands

Table 1
Summary of Flash Extent Density Altitude Distribution Statistics for the Three cases

Altitude (km)	Case I IQR	Case I mean	Case II IQR	Case II mean	[a]Case III mean
5	0.09	1.15	0.05	1.07	1.00
6	0.12	1.19	0.07	1.13	1.01
7	0.12	1.24	0.09	1.18	1.01
8	0.14	1.27	0.15	1.21	1.02
9	0.14	1.28	0.13	1.24	1.03
10	0.13	1.31	0.20	1.31	1.03
11	0.19	1.35	0.36	1.34	1.02
12	0.21	1.35	0.31	1.32	1.03
13	0.19	1.35	0.32	1.31	1.02
14	0.17	1.37	0.25	1.32	1.00
15	0.23	1.46	0.29	1.36	1.00

Note. The heights range from the melting layer to just below the tropopause. Note that lightning activity above this level is not considered. The interquartile range (IQR) is calculated by subtracting the 75th and 25th percentiles. The mean flash extent density heights are also provided. [a]Case III did not have enough data points other than unity in which to calculate the IQR, hence only the mean values are provided.

that developed over the Houston Metropolitan area during a 2-day period (August 26, 2017–August 27, 2017). The rain bands were also responsible catastrophic flooding in the region (~700 mm of rain). Two primary conclusions from three notable cases are presented to address SQ1 and SQ2:

SQ1) The dynamic/thermodynamic environment consisted of high SBCAPE (~1,800 J kg^{-1}), weak shear (<10 m s^{-1}), and abundant moisture (PWV ~ 60 mm). As Harvey propagated eastward, southeasterly winds continuously advected moisture from the Gulf of Mexico. In addition, a southward moving stationary front interacted with Harvey and likely provided an additional lifting mechanism of the moist air parcels. As a result, an intense, convective feeder band developed and stalled over the Houston Metropolitan area on August 26, 2017–August 27, 2017. Case I occurred during the late evening hours of August 26, 2017 (0200 UTC August 2017) within the main area of feeder band convection while Case II (0500 UTC) evolved from a mini-supercell thunderstorm after 0500 UTC August 27, 2017 that produced two EF1 rated tornadoes. After 1100 UTC, a broad area of intense shallow convection caused extreme flooding east of the Houston Metropolitan Area during Case III.

SQ2) Case I exhibited the highest peak lightning flash rate of ~18,000 flashes (30 min)$^{-1}$, peak lightning flash extent density of 12.4 km^{-2} min^{-1}. The peak rain rate was 6.5 mm hr^{-1}. Peak reflectivities were in excess of 50 dBZ and the maximum 30 dBZ echo height was collocated with a flash extent density peak of 2.6 km^{-2} min^{-1} at ~15 km. Case II exhibited a lightning flash rate of ~10,300 flashes (30 min)$^{-1}$ and a comparable peak lightning flash extent density of 9.9 km^{-2} min^{-1} and peak rain rate of 5.6 mm hr^{-1}. In addition, there was a similar collocation of 30 dBZ echo height and flash extent density peak (3.2 km^{-2} min^{-1}) at an altitude of ~15 km. Note that the flash density of Case II (smaller cell) was comparable to the flash density of the larger convective feeder band analyzed in Case I which suggests enhanced microphysics. Hence, this will serve as a focus for future research involving aerosol-cloud-lightning interactions.

Cases I and II had regions of positive Z_{dr} (k_{dp}) dual-pol values exceeding 2 dB (deg km^{-1}) indicating vigorous updrafts and intense precipitation at the surface. Moreover, there were regions of negative Z_{dr} (k_{dp}) values ~−0.15 dB (deg km^{-1}) that were not only located above the areas of intense rainfall but were also collocated with the areas of intense lightning flash activity. This (a) suggested the presence of vertically oriented ice particles and (b) provided some clues to the location and evidence of the charging regions responsible for the enhanced lightning observed during Cases I and II.

Prior to Case III, at 0900 UTC the rain rate peaked at 14.2 mm hr^{-1} and the lightning flash rate was ~6900 flashes (30 min)$^{-1}$ while the HLMA flash height decreased below 10 km. During Case III, the 30 dBZ reflectivity echo height declined to below 6 km while the peak lightning flash extent density was roughly 1.5 km^{-2} min^{-1} after 1100 UTC. There was a further decline in the lightning flash rate (~100 [30 min]$^{-1}$) while the rain rate was nearly 8 mm hr^{-1} suggesting a transition to shallow convection. The Z_{dr} (k_{dp}) dual-pol products for Case III ranged between 1 and 1.5 dB (deg km^{-1}) below the melting layer which indicated moderately strong updrafts and heavy precipitation near the surface. Above the melting layer, the values seldom exceeded 0.5 dB (deg km^{-1}) indicating weaker updrafts and fewer ice particles aloft.

The lightning activity from the eyewall (>250 km from the centroid) was well captured by the HLMA prior to and during landfall. Hence, future work will investigate Harvey eyewall lightning activity using the flash extent density which has proven quite useful in this study.

It is the competition between cold rain (ice process) and warm rain (collision-coalescence) mechanisms within tropical cyclones that is, difficult to reconcile by using lightning alone. However, lightning is indeed an adequate predictor of extreme deep convective behavior when the mixed-phase depth and height of the 30 dBZ echo are sufficiently elevated, which in the case of a tropical cyclone like Harvey, was atypical.

Table 2
Summary of the Dual-Polarization Product Values Below and Above the Melting Layer (4.6 km) for the Three Cases

	Case I	Case II	Case III
Below melting layer	0140–0150 UTC	0505–0515 UTC	1150–1200 UTC
k_{dp} (deg km^{-1})	2.0–2.5[a]	>2.75[a]	0.75–1.0
Z_{dr} (dB)	1.0–1.5[a]	~2.0[a]	1.25–1.5
i$_{hv}$	~0.98	~0.98	~0.98
Above melting layer	0140–0150 UTC	0505–0515 UTC	1150–1200 UTC
k_{dp} (deg km^{-1})	~0.25	~1	0–0.25
Z_{dr} (dB)	<−0.15[b]	<−0.15[b]	~0.5
ρ_{hv}	~0.98	0.88–0.96[b]	~0.98

[a]Maximum near-surface values. [b]Mininum mid- and upper troposphere values.

Hence, the HLMA network will be used in future studies to provide both a baseline and climatology of lightning behavior of convection that develops in a transitional marine/continental environment (e.g., air mass and sea breeze thunderstorms, deep convection initiated by synoptic fronts, and tropical cyclones). Moreover, the Houston Metropolitan Area is a main source region of urban/industrial aerosols which are known to impact cloud microphysics and electrification. Thus, the HLMA will be beneficial in examining the nature of convection that may have been perturbed by aerosols in future research opportunities.

Data Availability Statement

The Houston Lightning Mapping Array sensor data are maintained by Texas A&M University under the direction of Timothy Logan and can be made available upon request. This study benefitted greatly from the Hurricane Harvey technical report provided by NOAA and available at https://www.weather.gov/hgx/hurricaneharvey. Additional meteorological data were provided by Plymouth State University (https://vortex.plymouth.edu/~wxp/sfc/). The geopotential height data used in Figure 1 was provided by the NOAA Physical Sciences Laboratory (https://psl.noaa.gov/data/composites/day/). NEXRAD data were obtained and processed using the NOAA Weather & Climate Toolkit application available at https://catalog.data.gov/dataset/noaa-weather-and-climate-toolkit-wct. The GridRad dataset was provided by Cameron Homeyer (https://gridrad.org). GPM data were provided by the NASA Giovanni data portal (https://giovanni.gsfc.nasa.gov/giovanni/)

References

Borque, P., Vidal, L., Rugna, M., Lang, T. J., Nicora, M. G., & Nesbitt, S. W. (2020). Distinctive signals in 1-min observations of overshooting tops and lightning activity in a severe supercell thunderstorm. *Journal of Geophysical Research: Atmospheres*, *125*, e2020JD032856. https://doi.org/10.1029/2020JD032856

Brauer, N. S., Basara, J. B., Homeyer, C. R., McFarquhar, G. M., & Kirstetter, P. E. (2020). Quantifying precipitation efficiency and drivers of excessive precipitation in post-landfall Hurricane Harvey. *Journal of Hydrometeorology*, *21*, 433–451. https://doi.org/10.1175/JHM-D-19-0192.1

Bruning, E. C., & MacGorman, D. R. (2013). Theory and observations of controls on lightning flash size spectra. *Journal of the Atmospheric Sciences*, *70*, 4012–4029. https://doi.org/10.1175/JAS-D-12-0289.1

Bruning, E., Tillier, C. E., Edgington, S. F., Rudlosky, S. D., Zajic, J., Gravelle, C., et al. (2019). Meteorological imagery for the geostationary lightning mapper. *Journal of Geophysical Research: Atmospheres*, *124*, 14258–14309. https://doi.org/10.1029/2019JD030874

Calhoun, K. M., MacGorman, D. R., Ziegler, C. L., & Biggerstaff, M. I. (2013). Evolution of lightning activity and storm charge relative to dual-Doppler analysis of a high-precipitation supercell storm. *Monthly Weather Review*, *141*(7), 2199–2223. https://doi.org/10.1175/MWR-D-12-00258.1

Carr, N., Kirstetter, P. E., Gourley, J. J., & Hong, Y. (2017). Polarimetric signatures of midlatitude warm-rain precipitation events. *Journal of Applied Meteorology and Climatology*, *56*, 697–711. https://doi.org/10.1175/JAMC-D-16-0164.1

Chmielewski, V. C., & Bruning, E. C. (2016). Lightning Mapping Array flash detection performance with variable receiver thresholds. *Journal of Geophysical Research: Atmospheres*, *121*, 8600–8614. https://doi.org/10.1002/2016JD025159

Cifelli, R., Chandrasekar, V., Lim, S., Kennedy, P. C., Wang, Y., & Rutledge, S. A. (2010). A new dual-polarization radar rainfall algorithm: application in Colorado precipitation events. *Journal of Atmospheric and Oceanic Technology*, *28*, 352–364. https://doi.org/10.1175/2010JTECHA1488.1

Cooney, J. W., Bowman, K. P., Homeyer, C. R., & Fenske, T. M. (2018). Ten-year analysis of tropopause-overshooting convection using GridRad data. *Journal of Geophysical Research*, *123*, 329–343. https://doi.org/10.1002/2017JD0277181

Crum, T. D., & Alberty, R. L. (1993). The WSR-88D and the WSR-88D operational support facility. *Bulletin of the American Meteorological Society*, *74*(9), 1669–1687. https://doi.org/10.1175/1520-0477(1993)074%3C1669:TWATWO%3E2.0.CO.2

Cui, W., Dong, X., Xi, B., Fan, J., Tian, J., Wang, J., et al. (2019). Understanding ice cloud-precipitation properties of three modes of mesoscale convective systems during PECAN. *Journal of Geophysical Research: Atmospheres*, *124*. https://doi.org/10.1029/2019JD030330

Cullen, M. R. (2013). *The Houston Lightning Mapping Array: Network installation and preliminary analysis*. Master's thesis. Texas A & M University. Available electronically from https://oaktrust.library.tamu.edu/handle/1969.1/151109

Cummins, K. L., & Murphy, M. J. (2009). An overview of lightning location systems: History, techniques, and data uses, with an in-depth look at the U. S. NLDN. *IEEE Transactions on Electromagnetic Compatibility*, *51*(3), 499–518. https://doi.org/10.1109/TEMC.2009.2023450

Cummins, K. L., Murphy, M. J., & Tuel, J. V. (2000). Lightning detection methods and meteorological applications. In IV international symposium on military meteorology hydro-meteorological support of allied forces and PfP members tasks realization. Poland: Malbork.

DeMaria, M., DeMaria, R. T., Knaff, J. A., & Molenar, D. (2012). Tropical cyclone lightning and rapid intensity change. *Monthly Weather Review*, *140*, 1828–1842.

DiGangi, E. A., MacGorman, D. R., Ziegler, C. L., Betten, D., Biggerstaff, M., Bowlan, M., et al. (2016). An overview of the 29 May 2012 Kingfisher supercell during DC3. *Journal of Geophysical Research: Atmospheres*, *121*, 14316–14343. https://doi.org/10.1002/2016JD025690

Fan, J., Liu, Y.-C., Xu, K.-M., North, K., Collis, S., Dong, X., et al. (2015). Improving representation of convective transport for scale-aware parameterization: 1. Convection and cloud properties simulated with spectral bin and bulk microphysics. *Journal of Geophysical Research: Atmospheres*, *120*, 3485–3509. https://doi.org/10.1002/2014JD022142

Fan, J., Zhang, R., Collins, D., & Li, G. (2006). Contribution of secondary condensable organics to new particle formation: A case study in Houston, Texas. *Geophysical Research Letters*, *33*, L15802. https://doi.org/10.1029/2006GL026295

Fridlind, A. M., van Lier-Walqui, M., Collis, S., Giangrande, S. E., Jackson, R. C., Li, X., et al. (2019). Use of polarimetric radar measurements to constrain simulated convective cell evolution: A pilot study with Lagrangian tracking. *Atmospheric Measurement Techniques*, *12*, 2979–3000. https://doi.org/10.5194/amt-12-2979-2019

Fuchs, B. R., Bruning, E. C., Rutledge, S. A., Carey, L. D., Krehbiel, P. R., & Rison, W. (2016). Climatological analyses of LMA data with an open-source lightning flash-clustering algorithm. *Journal of Geophysical Research: Atmospheres*, *121*, 8625–8648. https://doi.org/10.1002/2015JD024663

Fuchs, B. R., & Rutledge, S. A. (2018). Investigation of lightning flash locations in isolated convection using LMA observations. *Journal of Geophysical Research: Atmospheres*, *123*(11), 6158–6174.

Fuchs, B. R., Rutledge, S. A., Bruning, E. C., Pierce, J. R., Kodros, J. K., Lang, T. J., et al. (2015). Environmental controls on storm intensity and charge structure in multiple regions of the continental United States. *Journal of Geophysical Research: Atmospheres*, *120*, 6575–6596. https://doi.org/10.1002/2015JD023271

Homeyer, C. R., & Bowman, K. P. (2017). *Algorithm description document for version 3.1 of the three-dimensional Gridded NEXRAD WSR-88D Radar (GridRad) dataset*. Technical Report. Retrieved from https://gridrad.org/pdf/GridRad-v3.1-Algorithm-Description.pdf

Koshak, W. J., Krider, E. P., Murray, N., & Boccippio, D. J. (2007). Lightning charge Retrievals: dimensional reduction, LDAR constraints, and a First comparison with LIS satellite data. *Journal of Atmospheric and Oceanic Technology*, *24*, 1817–1838. https://doi.org/10.1175/JTECH2089.1

Kumjian, M. R. (2013). Principles and applications of dual-polarization weather radar. Part I: Description of the polarimetric radar variables. *Journal of Operational Meteorology*, *1*(19), 226–242. https://dx.doi.org/10.15191/nwajom.2013.0119

Levy, M. E., Zhang, R., Khalizov, A. F., Zheng, J., Collins, D. R., Glen, C. R., et al. (2013). Measurements of submicron aerosols in Houston, Texas during the 2009 SHARP field campaign. *Journal of Geophysical Research: Atmospheres*, *118*, 10518–10534. https://doi.org/10.1002/jgrd.50785

Li, X., & Mecikalski, J. R. (2012). Impact of the dual-polarization Doppler radar data on two convective storms with a warm-rain radar forward operator. *Monthly Weather Review*, *140*, 2147–2167. https://doi.org/10.1175/MWR-D-11-00090.1

Logan, T. (2018). Anomalous lightning behavior during the 26–27 August 2007 Northern Great Plains severe weather event. *Journal of Geophysical Research: Atmospheres*, *123*. https://doi.org/10.1002/2017JD027750

Lyons, W. A., Nelson, T. E., Williams, E. R., Cramer, J. A., & Turner, T. R. (1998). Enhanced positive cloud-to-ground lightning in thunderstorms ingesting smoke from fires. *Science*, *282*(5386), 77–80. https://doi.org/10.1126/science.282.5386.77

McCaul, E. W., Goodman, S. J., LaCasse, K. M., & Cecil, D. J. (2009). Forecasting lightning threat using cloud-resolving model simulations. *Weather and Forecasting*, *24*(3), 709–729.

Mecikalski, R. M., & Carey, L. D. (2018). Radar reflectivity and altitude distributions of lightning flashes as a function of three main storm types. *Journal of Geophysical Research: Atmospheres*, *123*(22), 12814–12828. https://doi.org/10.1029/2018JD029238

Orville, R. E., Huffines, G., Nielsen-Gammon, J., Zhang, R., Ely, B., Steiger, S., et al. (2001). Enhancement of cloud-to-ground lightning over Houston, Texas. *Geophysical Research Letters*, *28*(13), 2597–2600.

Ren, T., Rapp, A. D., Nasiri, S. L., Mecikalski, J. R., & Apke, J. (2018). Is the awareness of the aerosol state useful in predicting enhanced lightning for lightning-producing storms over Northern Alabama? *Journal of Applied Meteorology and Climatology*, *57*, 1663–1681. https://doi.org/10.1175/JAMC-D-17-0182.1

Rison, W., Thomas, R. J., Krehbiel, P. R., Hamlin, T., & Harlin, J. (1999). A GPS-based three-dimensional lightning mapping system: Initial observations in central New Mexico. *Geophysical Research Letters*, *26*, 3573–3576. https://doi.org/10.1029/1999GL010856

Saunders, C. (1993). A review of thunderstorm electrification process. *Journal of Applied Meteorology*, *32*, 642–655.

Shao, X. M., Harlin, J., Stock, M., Stanley, M., Regan, A., Wiens, K., et al. (2005). Katrina and Rita were lit up with lightning. *Eos*, *86*(42), 398–399.

Skofronic-Jackson, G., Kirschbaum, D., Petersen, W., Huffman, G., Kidd, C., Stocker, E., et al. (2018). The Global Precipitation Measurement (GPM) mission's scientific achievements and societal contributions: reviewing four years of advanced rain and snow observations. *Quarterly Journal of the Royal Meteorological Society*, *144*(1), 27–48. https://doi.org/10.1002/qj.3313

Solomon, R., & Baker, M. (1998). Lightning flash rate and type in convective storms. *Journal of Geophysical Research*, *103*(D12), 14041–14057. https://doi.org/10.1029/97JD03323

Solomon, D. L., Bowman, K. P., & Homeyer, C. R. (2016). Tropopause-penetrating convection from three-dimensional gridded NEXRAD data. *Journal Applied Meteorology and Climatology*, *55*, 465–478. https://doi.org/10.1175/JAMC-D-15-0190.1

Solorzano, N. N., Thomas, J. N., & Bracy, C. (2018). Monitoring tropical cyclones with lightning and satellite data. *Eos*, *99*. https://doi.org/10.1029/2018EO092439

Solorzano, N. N., Thomas, J. N., Hutchins, M. L., & Holzworth, R. H. (2016). WWLLN lightning and satellite microwave radiometrics at 37 to 183 GHz: Thunderstorms in the broad tropics. *Journal of Geophysical Research: Atmospheres*, *121*, 12298–12318. https://doi.org/10.1002/2016JD025374

Starzec, M., Homeyer, C. R., & Mullendore, G. L. (2017). Storm Labeling in 3 Dimensions (SL3D): A volumetric radar echo and dual-polarization updraft classification algorithm. *Monthly Weather Review*, *145*, 1127–1145. https://doi.org/10.1175/MWR-D-16-0089.1

Stolz, D. C., Businger, S., & Terpstra, A. (2014). Refining the relationship between lightning and convective rainfall over the ocean. *Journal of Geophysical Research:Atmospheres*, *119*, 964–981. https://doi.org/10.1002/2012JD018819

Takahashi, T. (1978). Riming electrification as a charge generation mechanism in thunderstorms. *Journal of the Atmospheric Sciences*, *35*, 1536–1548.

Thomas, R. J., Krehbiel, P. R., Rison, W., Hunyady, S. J., Winn, W. P., Hamlin, T., et al. (2004). Accuracy of the lightning mapping array. *Journal of Geophysical Research*, *109*, D14207. https://doi.org/10.1029/2004JD004549

Thornton, J. A., Virts, K. S., Holzworth, R. H., & Mitchell, T. P. (2017). Lightning enhancement over major oceanic shipping lanes. *Geophysical Research Letters*, *44*, 9102–9111. https://doi.org/10.1002/2017GL074982

Tian, J., Dong, X., Xi, B., & Feng, Z. (2020). Characteristics of ice cloud-precipitation of warm season mesoscale convective systems over the Great Plains. *Journal of Hydrometeorology*, *21*, 317–334. https://doi.org/10.1175/JHM-D-19-0176.1

van Lier-Walqui, M., Fridlind, A. M., Ackerman, A. S., Collis, S., Helmus, J., MacGorman, D. R., et al. (2016). On polarimetric radar signatures of deep convection for model evaluation: Columns of specific differential phase observed during MC3E. *Monthly Weather Review*, *144*, 737–758. https://doi.org/10.1175/MWR-D-15-0100.1

Weiss, S. A., MacGorman, D. R., Bruning, E. C., & Chmielewski, V. C. (2018). Two methods for correcting range-dependent limitations of lightning mapping arrays. *Journal of Atmospheric and Oceanic Technology*, *35*, 1273–1282. https://doi.org/10.1175/JTECH-D-17-0213.1

Wiens, K. C., Rutledge, S. A., & Tessendorf, S. A. (2005). The 29 June 2000 Supercell Observed during STEPS. Part II: Lightning and Charge Structure. *Journal of the Atmospheric Sciences*, *62*, 4151–4177.

Xu, W., Rutledge, S. A., & Zhang, W. (2017). Relationships between total lightning, deep convection, and tropical cyclone intensity change. *Journal of Geophysical Research: Atmospheres*, *122*, 7047–7063. https://doi.org/10.1002/2017JD027072

Zhang, Y., Fan, J., Logan, T., Li, Z., & Homeyer, C. R. (2019). Wildfire impact on environmental thermodynamics and severe convective storms. *Geophysical Research Letters*, *46*, 10082–10093. https://doi.org/10.1029/2019GL084534

Zhang, W., Zhang, Y., Zheng, D., Wang, F., & Xu, L. (2015). Relationship between lightning activity and tropical cyclone intensity over the northwest Pacific. *Journal of Geophysical Research: Atmospheres*, *120*, 4072–4089. https://doi.org/10.1002/2014JD022334